*Original Paper*

# Field Measurements of Compaction Seepage Characteristics in Longwall Mining Goaf

Cun Zhang [1,2,4] Shihao Tu,[3] and Lei Zhang[3]

The spatiotemporal evolution of goaf caving zone compaction characteristics has important influences on surface subsidence, spontaneous combustion and gas and water migration characteristics in goaf. In this paper, the permeability of the caving zone during the advance of a longwall face is calculated based on the permeability calculation model and gas drainage data; additionally, the compaction stress and compaction time of goaf are measured by a borehole stress meter. The internal relations among compaction stress, compaction time and permeability at different positions in the caving zone are quantitatively analyzed. The results show that the farther away from the boundary of the caving zone, the lower the permeability, the greater the compaction stress and the longer the compaction time are. It is also confirmed by numerical simulation results. At the same time, the distribution characteristics of and quantitative relationships among compaction stress, compaction time and permeability are given. In addition, compaction time increases with the increase in the rate of advance of the longwall face, but the change is not large. Based on the above study, the space–time evolution of gob compaction characteristics is preliminarily grasped, which provides theoretical guidance for designing pressure relief gas drainage boreholes and the longwall face layouts.

## INTRODUCTION

Longwall mining technology, as an efficient mining method in coal seam mining, is widely used. With the continuous advancement of the longwall face, the overlying strata are broken to form the traditional four vertical zones. There are caving zone, fractured zone, bending zone and surface subsidence zone from longwall face to the surface. Among them, the caving zone is generally composed of broken rock and residual coal with high porosity (Palchik 2003, 2010; Cheng et al. 2017). Thus, abundant water and gas from adjacent strata flow into the caving zone along the rock strata fracture (Wang et al. 2015; Meng et al. 2016a). Besides, the residual coal in caving zone experiences long-term exposure to the air and is prone to spontaneous combustion, resulting in a large number of dangerous and harmful gases (Li et al. 2008; Zhao et al. 2008; Qin et al. 2015). The mechanical and physical properties of the caving zone including permeability, porosity, modulus, Poisson ratio and density will

[1] State Key Laboratory of Coal Resources and Safe Mining, China University of Mining and Technology (Beijing), Beijing 100083, China.
[2] School of Energy and Mining Engineering, China University of Mining and Technology (Beijing), Beijing 100083, China.
[3] School of Mines, Key Laboratory of Deep Coal Resource Ministry of Education of China, China University of Mining and Technology, Xuzhou 221116, Jiangsu, China.
[4] To whom correspondence should be addressed; e-mail: cumt-zc@cumtb.edu.cn

change accordingly as it is gradually compacted, which is caused by overlying strata pressure and its own gravity. The porosity and permeability of caving zone will gradually decrease with the increase in stress and strain, while the modulus, density and Poisson ratio will increase (Salamon 1991; Jozefowicz 1997; Yavuz 2004; Karacan 2010; Booth and Greer 2011; Liang et al. 2016). In the process of mining disturbance, the re-damage of the broken rock, the adjustment of pore structure and the deformation of the broken rock are the main factors causing the caving zone permeability change. The constant changes in the pore and flow characteristics of the caving zone will cause the spatiotemporal evolution of seepage in caving zone to be difficult to grasp, which affect mine safety production and utilization of water and gas resources in caving zone (Schatzel et al. 2012; Liu et al. 2015; Xia et al. 2015; Zhang et al. 2019). Moreover, because of the inhomogeneity of broken rock and the superposition of internal initial damage–water damage–stress damage, it is very difficult to accurately describe the deterioration process and failure mechanism of broken rock under the effect of mining and water–rock interaction by traditional methods.

Thus, a great deal of research on this topic has been carried out by scholars. The Carman–Kozeny and Happel equations can be used to calculate the permeability of caving zone. According to these two equations, the fractal permeability model has been proposed, whereby the porosity and permeability can be predicted with the size distribution of broken rock block in the caving zone (Li and Logan 2001; Karacan 2010). Some semiempirical formulas based on the experimental results have been proposed to calculate stress changes in the process of caving compaction. Salamon formula indicated that the compaction stress in the caving zone exponentially increases with the increase in strain (Salamon 1991). The permeability model describing the pore structure of broken rock mass from formation to compaction stability was proposed by Fan and Liu (2017). In this model, the secant modulus of the whole model was changed in each stage during the caving zone compaction, and there is no particle size parameter in the model, which greatly simplified the calculation difficulty. However, direct field measurements of compaction permeability and stress in the caving zone are difficult to make. Thus, field measurements of caving zone permeability and stress were especially rarely reported.

The main field measurements are focused on the caving zone height (Barrash et al. 2006; Baptiste and Chapuis 2015). The statistical change in surface subsidence after coal seam mining can be used to indirectly calculate the caving zone compaction degree (Deng et al. 2012; Zhu et al. 2014). A gas flow rates calculation model was established by Zhou et al. (2010). It can forecast the gas flow rates extraction from caving zone based on the conservation of mass. This model was then simplified by using comprehensive measured data to calculate the caving zone permeability (Zhang et al. 2016). In addition to the difficulty of measurement, the above analysis rarely considers the compaction time of the caving zone.

Therefore, accurately grasping the spatiotemporal evolution of goaf caving zone compaction and seepage characteristics has important influences on the development and utilization of the caving zone resources and the safe and efficient mining of the coal mines. In this paper, the permeability of the caving zone during longwall face advancing is calculated based on the permeability calculation model and gas drainage data of the gob gas venthole (GGV); additionally, the compaction stress of the caving zone is measured. The internal relations among compaction stress, compaction time and permeability at caving zone different positions are quantitatively analyzed. Combined with the above study, the space–time evolution of caving zone compaction characteristics is preliminarily grasped, which provides theoretical guidance for designing pressure relief gas drainage boreholes and longwall face layouts.

## ENGINEERING GEOLOGICAL CONDITIONS

The caving zone in the longwall face LW1112 (1) is the study area of this paper. The strike length of this longwall face was 2181.8 m, and the dip length was 220 m. Figure 1 shows the details of the LW1112 (1) panel. The average cover depth and mining thickness of LW1112 (1) panel are 950 m and 1.2 m, respectively, and located on the 11–2 coal seam. The mechanical property of the rock and coal in the Huainan coalfield is shown in Table 1. To remove the outburst danger of the 13-1 coal seam (the gas pressure is 3.7 MPa) and pre-extract the coal seam gas, the 11–2 coal seam (the gas pressure is 0.5 MPa) was mined first. Meanwhile, compre-
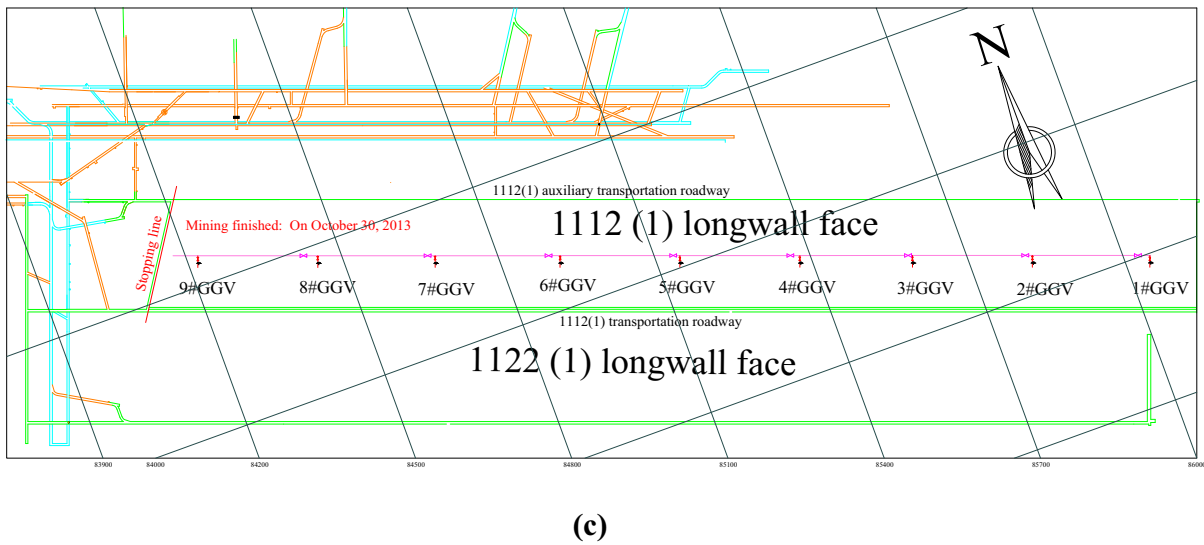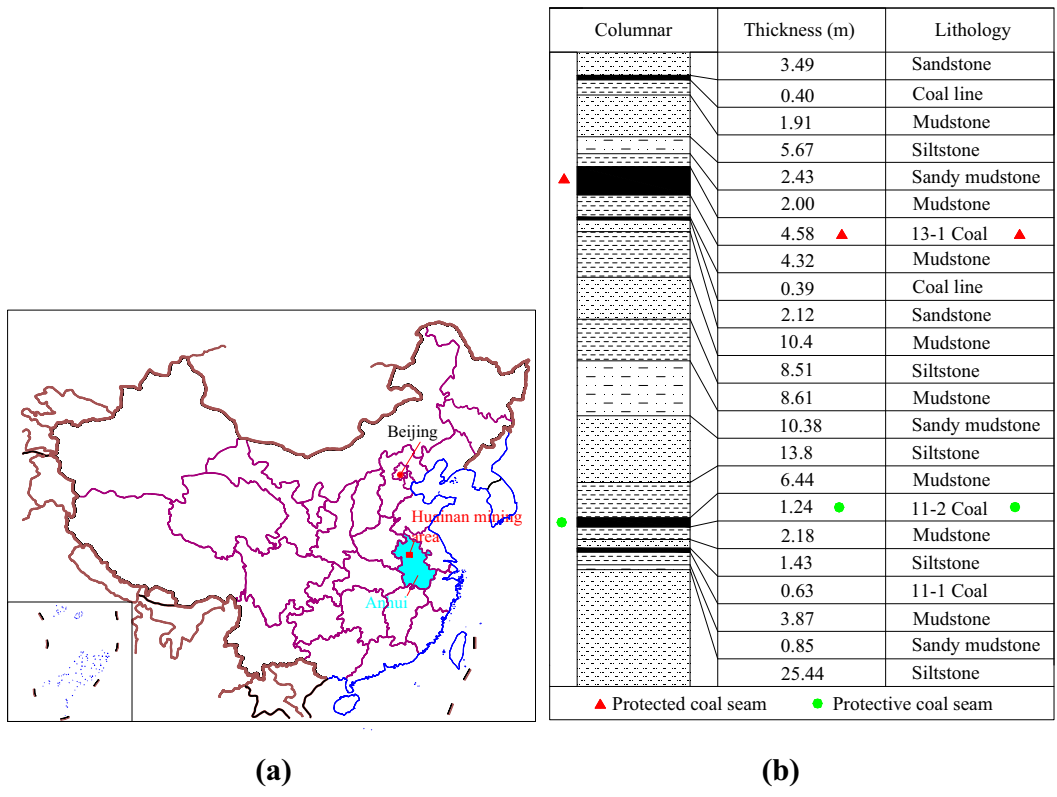
| Columnar | Thickness (m) | Lithology |
|---|---|---|
| | 3.49 | Sandstone |
| | 0.40 | Coal line |
| | 1.91 | Mudstone |
| | 5.67 | Siltstone |
| ▲ | 2.43 | Sandy mudstone |
| | 2.00 | Mudstone |
| | 4.58 ▲ | 13-1 Coal ▲ |
| | 4.32 | Mudstone |
| | 0.39 | Coal line |
| | 2.12 | Sandstone |
| | 10.4 | Mudstone |
| | 8.51 | Siltstone |
| | 8.61 | Mudstone |
| | 10.38 | Sandy mudstone |
| | 13.8 | Siltstone |
| | 6.44 | Mudstone |
| ● | 1.24 ● | 11-2 Coal ● |
| | 2.18 | Mudstone |
| | 1.43 | Siltstone |
| | 0.63 | 11-1 Coal |
| | 3.87 | Mudstone |
| | 0.85 | Sandy mudstone |
| | 25.44 | Siltstone |

▲ Protected coal seam  ● Protective coal seam



**(a)**

**(b)**



**(c)**

**Figure 1.** Details of the LW1112(1) panel in the Huainan coalfield: (**a**) the Huainan coalfield location in China; (**b**) the borehole diagram of the longwall face; and (**c**) the details of LW1112(1) panel.

hensive pressure relief methane extraction technologies including GGV, crossing seam drilling hole (CSDH), large diameter horizontal long drilling hole (LDHLDH) and buried pipe for extraction (BPE) were used to promote safe and efficient mining of the LW1112 (1) and extract the pressure relief gas from the 13-1 coal seam (Fig. 2) (Zhang et al. 2017). Thus, understanding the properties of the caving

**Table 1.** Mechanical property of rock and coal in the Huainan coalfield

| Coal measures | Bulk modulus (GPa) | Shear modulus (GPa) | Cohesion (MPa) | Friction angle (°) | Tensile strength (MPa) |
|---|---|---|---|---|---|
| 11-2 coal | 1.33 | 1.61 | 2.10 | 30.00 | 1.00 |
| 13-1 coal | 0.69 | 0.75 | 1.14 | 37.13 | 1.09 |
| Siltstone | 28.02 | 20.71 | 12.20 | 38.93 | 6.15 |
| Mudstone | 12.65 | 16.19 | 8.00 | 32.07 | 4.30 |
| Sandstone | 32.46 | 28.42 | 15.56 | 37.25 | 8.80 |
| Sandy mudstone | 16.65 | 8.99 | 8.50 | 35.12 | 4.50 |

zone compaction seepage characteristics is very important to optimize the extraction venthole parameters and placement.

## Permeability Evolution Characteristics of Caving Zone

At present, the permeability, porosity, methane content and concentration in goaf were usually calculated by theoretical model and numerical simulation due to the difficulties in field measurement. Therefore, the theoretical model based on the gas drainage data obtained from GGV was proposed by many researchers (Lan and Zhang 2007; Meng et al. 2016b). A gas flow rates ($v_0$) calculation model was established by Zhou et al. (2010), based on the conservation of mass. This equation was then simplified by Zhang et al. (2015) with the basic parameters of gas extraction data; there are $c$ (gas concentration, %), $d$ (diameter of the venthole, m), $v$ (average flow rate, m/s), $\rho$ (density of pure gas, kg/m$^3$), $h_0$ (height of caving zone, m) and $\rho_k$ (density of air under standard conditions, kg/m$^3$), as expressed in Eq. 1.

$$v_0 = \frac{d(-1+c_2)v_2(-\rho_k + c_2\rho_k - \rho c_2)}{4(-1+c_0)h_0(-\rho_k + c_0\rho_k - \rho c_0)} = K \times \frac{\Delta P}{l} \quad (1)$$

In Eq. 1, the subscripts 2 and 0 correspond to the section label of surface and caving zone in Figure 3. According to Darcy's law, the pressure difference ($\Delta P$) and effective extraction radius ($l$) allow for the evolution characteristics of the caving zone permeability to be obtained (Zhang et al. 2016). According to the monitoring data of gas extraction during LW1112 (1) mining, the evolution law of permeability in the caving zone can be calculated (Fig. 4). There are two stages (decline stage and the stable stage) of permeability evaluation during the GGV extraction. The first decline stages of 1# GGV,

2# GGV, 3# GGV, 4 # GGV, 5# GGV and 6# GGV last for 31 d, 45 d, 49 d, 55 d, 53 d and 54 d, respectively. The average duration is 47.8 d. The corresponding advancing distances of LW1112 (1) at the decline stage were 232 m, 303 m, 331 m, 358 m, 328 m and 289 m, respectively, with an average distance of 306.8 m.

The decrease in permeability in the goaf caving zone is mainly due to the gradual compaction of the caving zone in the goaf. In addition to the LW1112 (1), the extraction data from the adjacent longwall face are also collected. The advancing distance from each longwall face to the caving zone stable stage and the time required are shown in Table 2. From Table 2, it can be seen that the average advancing distance for the caving zone reaching the stable stage of each longwall face is quite different. The maximum average advancing distance is 306.8 m for LW1112 (1) and the smallest is 205.2 m for LW1242 (1), which account for the largest 66.8% of the measured advancing distances. However, there is little difference in the compacting time of each longwall face. The maximum is 47.8 d for LW1112 (1) and the smallest is 43.2 d for LW1242 (1), which account for the largest 90.4% of measured compacting times. This is mainly due to the large difference in the advancing speed of each longwall face; that is, with the same compaction time, the greater the advancing speed is, the longer the advancing distance of the longwall face is. The larger the advancing speed is, the longer the time needed for the complete compaction of the caving zone is. However, this effect is small (Fig. 5). Thus, in the process of the longwall face advancing, the compaction time of the caving zone more accurately measures the compaction degree than the advancing distance.

In addition, for each longwall face, there are differences in compaction time in different regions of the caving zone, and the closer the distance from
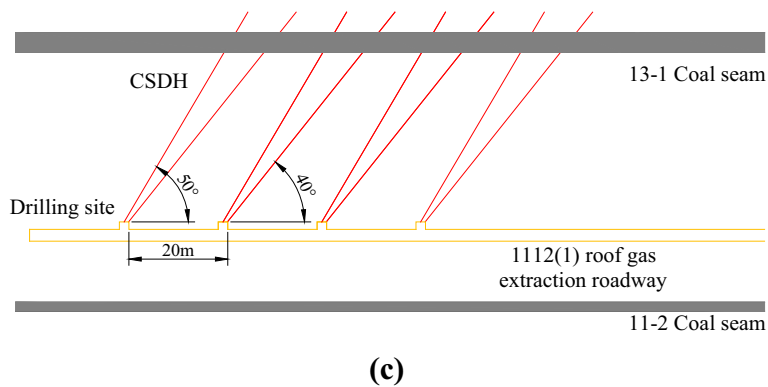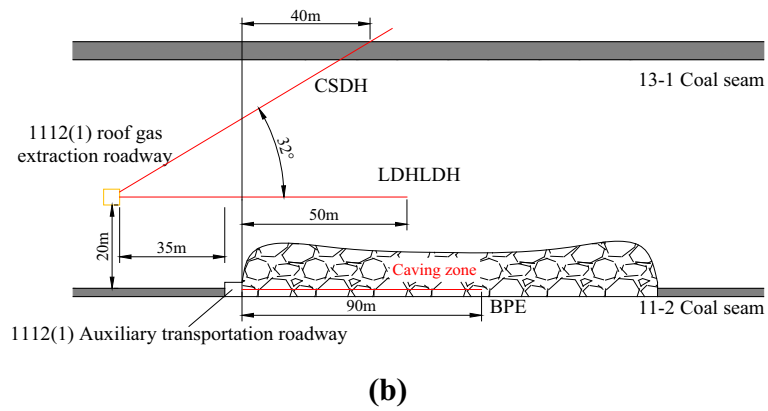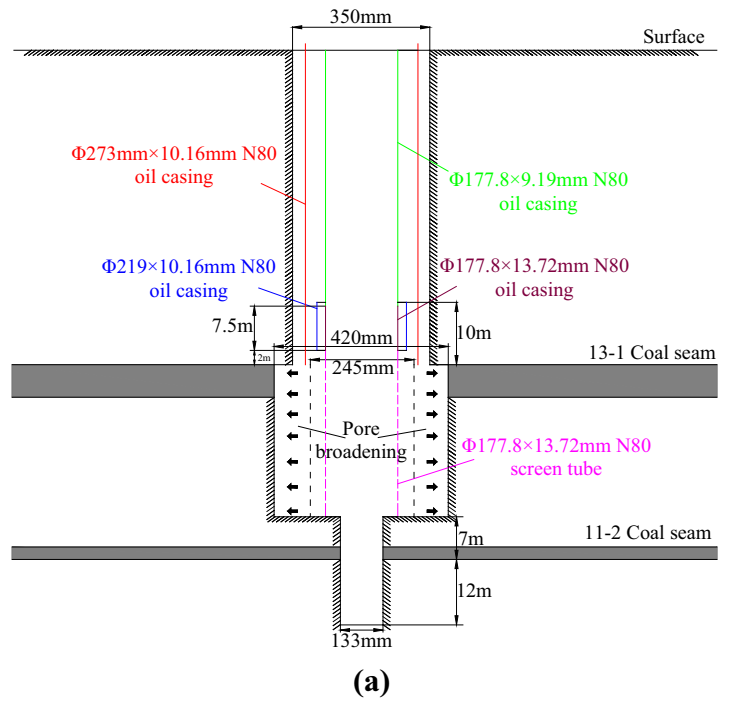
**(a)**



**(b)**



**(c)**

**Figure 2.** Schematic diagram of overburden strata and comprehensive pressure relief methane extraction technologies: (**a**) GGV; (**b** and **c**) CSDH, LDHLDH and BPE.
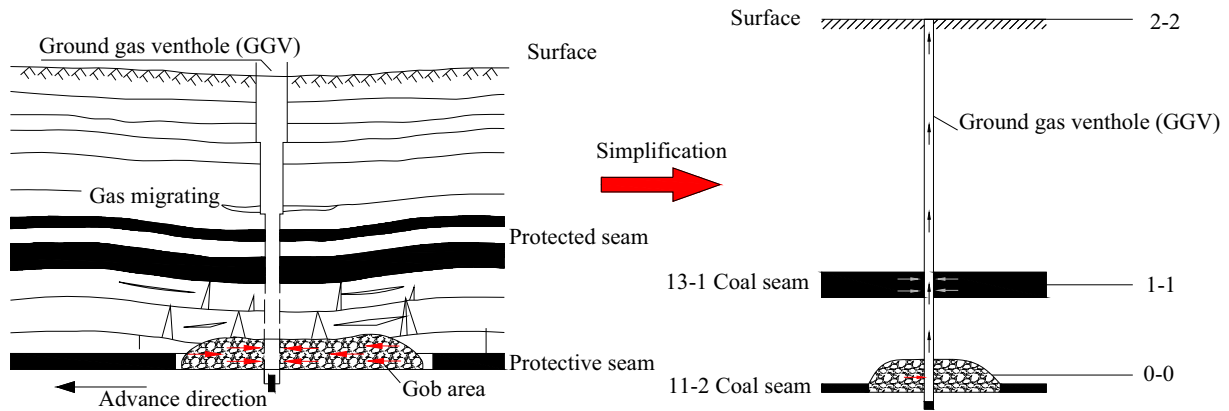
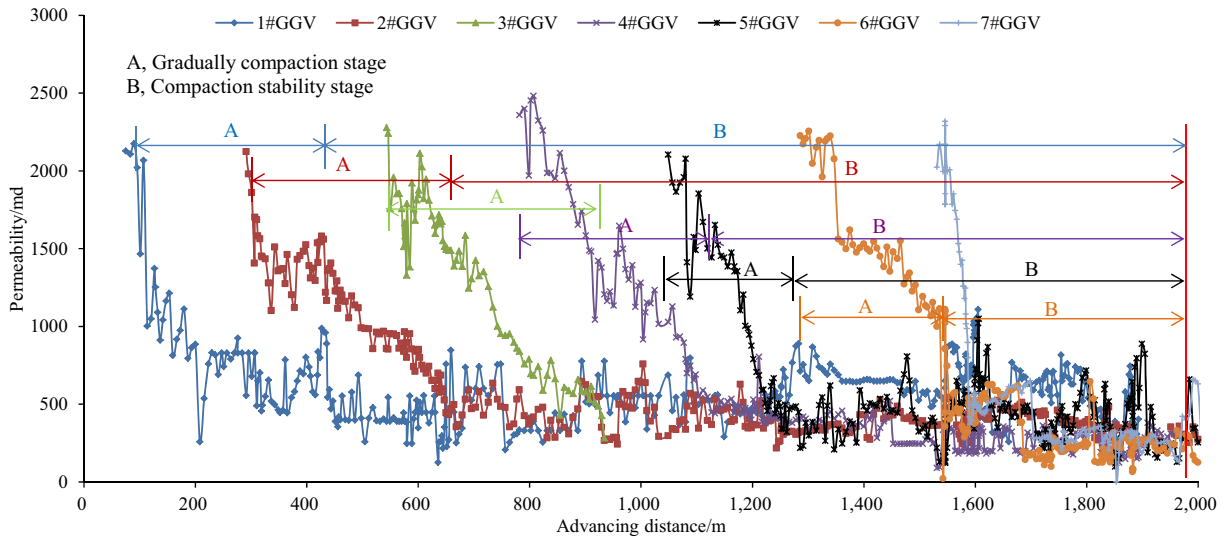**Figure 3.** Model of gas flow rates from different sources in a drilling well.



**Figure 4.** Permeability evolution curve of the caving zone around the GGV during its compaction.

**Table 2.** Distance and experienced times of various stages of permeability

| Longwall face | 1#GGV | 2# GGV | 3# GGV | 4# GGV | 5# GGV | 6# GGV | Average |
|---|---|---|---|---|---|---|---|
| 1111 (1) | 203 m/33 d | 228 m/42 d | 278 m/52 d | 259 m/54 d | 231 m/47 d | Unclear | 237.8 m/45.6 d |
| 1112 (1) | 232 m/31 d | 303 m/45 d | 331 m/49 d | 358 m/55 d | 328 m/53 d | 289 m/54 d | 306.8 m/47.8 d |
| 1121 (1) | 164 m/28 d | 219 m/43 d | 245 m/50 d | 265 m/51 d | 240 m/46 d | 235 m/50 d | 228.0 m/44.7 d |
| 1242 (1) | 125 m/28 d | 189 m/41 d | 235 m/47 d | 259 m/52 d | 218 m/48 d | Unclear | 205.2 m/43.2 d |

the open-off cut is, the shorter the required compaction time is. This is mainly due to the difference in the compaction degree in each area of the caving zone. The closer to the caving zone boundary, the

lower the vertical stress is and the lower the compaction time needed. To study the specific distribution of permeability in the caving zone after the longwall face finishes advancing, this paper calcu-
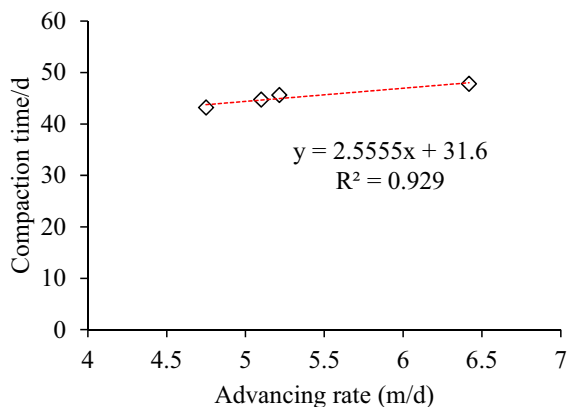
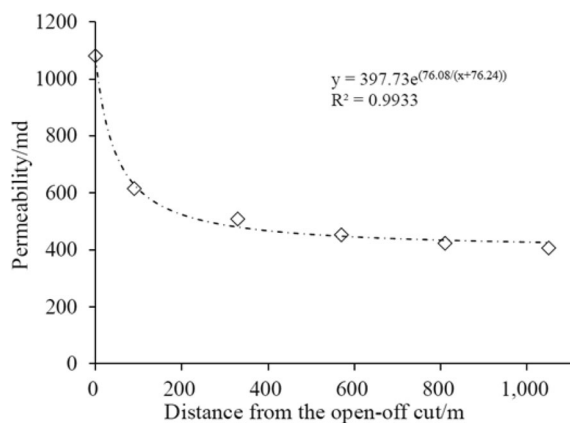**Figure 5.** Relationship between compaction time and longwall face advance rate.



**Figure 6.** Calculation method of permeability in fully compacted gob.

lated the permeability of each GGV during the stable stage. Figure 6 shows the permeability of 1-5# GGV (5# GGV was located at the center of the caving zone) in LW1112 (1) at different distances from the open-off cut. As seen from the figure, the farther away from the open-off cut, the lower the permeability is, and the permeability is sharply reduced at the edge of the caving zone. There is a negative relationship between distance from the open-off cut and permeability. This relationship is caused by the following two reasons: (1) the vertical stress increases sharply at the edge of the caving zone and (2) the stress sensitivity of the permeability decreases with the increase in stress. The contour map of the permeability distribution of the caving zone is shown in Figure 7 using SUFFER drawing software.

## Compacted Stress Evolution Characteristics of Caving Zone

To further study the compaction stress and compacting time of the caving zone, the vertical stress in the compaction process is measured using KS-II stress meter (Fig. 8c). The location of each monitoring point in the caving zone is shown in Figure 8. Due to the symmetry of the longwall face, the monitoring points are arranged with respect to the central 5# GGV in the advancing direction, and the measuring point is arranged around each GGV and in the middle of each two adjacent GGVs. In the longwall face direction, two row monitoring points are arranged near the open-off cut (the beginning of longwall face mining) and the 5# GGV. Each borehole stress meter is arranged in the gob side entry retaining. The monitoring results are shown in Figure 9. The assumption is that the roof at the edge of the caving zone does not cave, and so the compaction time and stress at this point are 0.

According to Figure 9, the compaction stress of the caving zone and the corresponding compaction time are closely related to the distance from the edge of the caving zone. The closer to the edge of the caving zone, the smaller the compacting stress is and the shorter the compaction time required to reach the stable stage. Based on the measured data of each monitoring point, the fitting formulas of compaction stress and compaction time at different distances from the edge of the caving zone are obtained (Fig. 9). From the correlation coefficients of $R^2 > 0.98$ of the fitting formulas, it can be seen that the negative exponential functions can appropriately describe the relationships between distance from the edge of the caving zone, compaction stress and compaction time. By using the fitting formulas and the difference algorithm, the compaction time and compaction stress at any point in the caving zone after it compacted can be calculated. The contour map of compaction time and compaction stress distribution of the caving zone is shown in Figure 10. In the figure, only half of the longwall face in the advancing direction is plotted.

The compaction time distribution of the caving zone is basically the same as that of the compaction stress, with high compaction stress corresponding to long compaction time. The compaction degree of the caving zone presents a horizontal "O"-type distribution, and the compaction degree from the inside to the outside is reduced in turn. The evolution characteristics of the compaction stress during
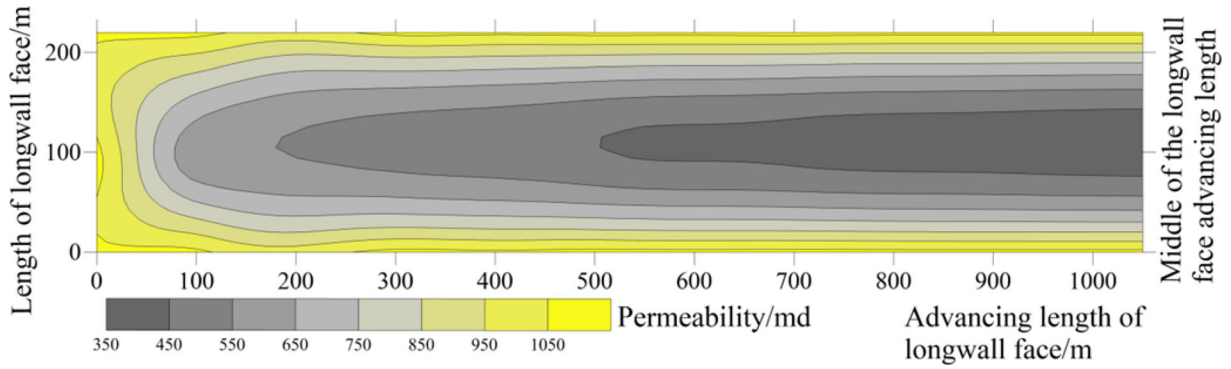
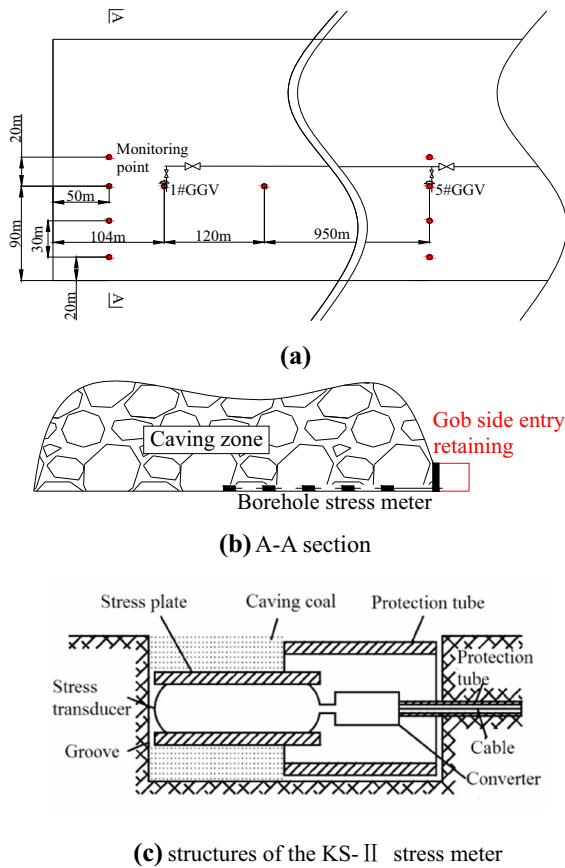**Figure 7.** Plan view of a longwall face showing distribution of permeability in fully compacted gob.



**(a)**

**(b)** A-A section

**(c)** structures of the KS-II stress meter

**Figure 8.** Layout of stress monitoring points in caving zone and structures of stress meter.



**(a)**

**(b)**

**Figure 9.** Relationship between compaction characteristics of caving zone and distance to boundary: (**a**) along strike; (**b**) along sloping direction.

compaction can also be simulated by the FLAC 3D program with FISH language using the Salamon formula (Salamon 1991). In this numerical simulation, the caving zone vertical stress can be calculated continuously by the caving zone vertical strain
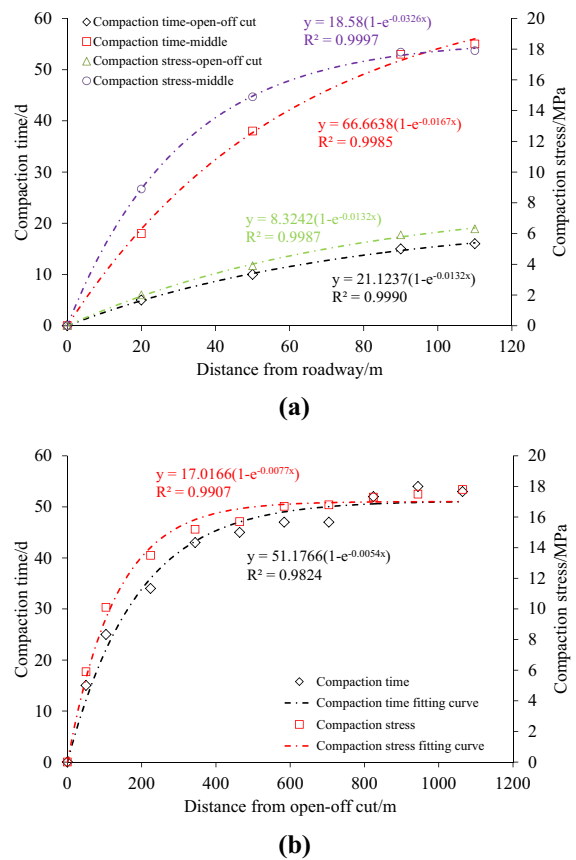
according to Eq. 2 (Whittles et al. 2006; Esterhuizen and Karacan 2007), and the simulation results of caving zone compaction stress in this paper are shown in Figure 11.
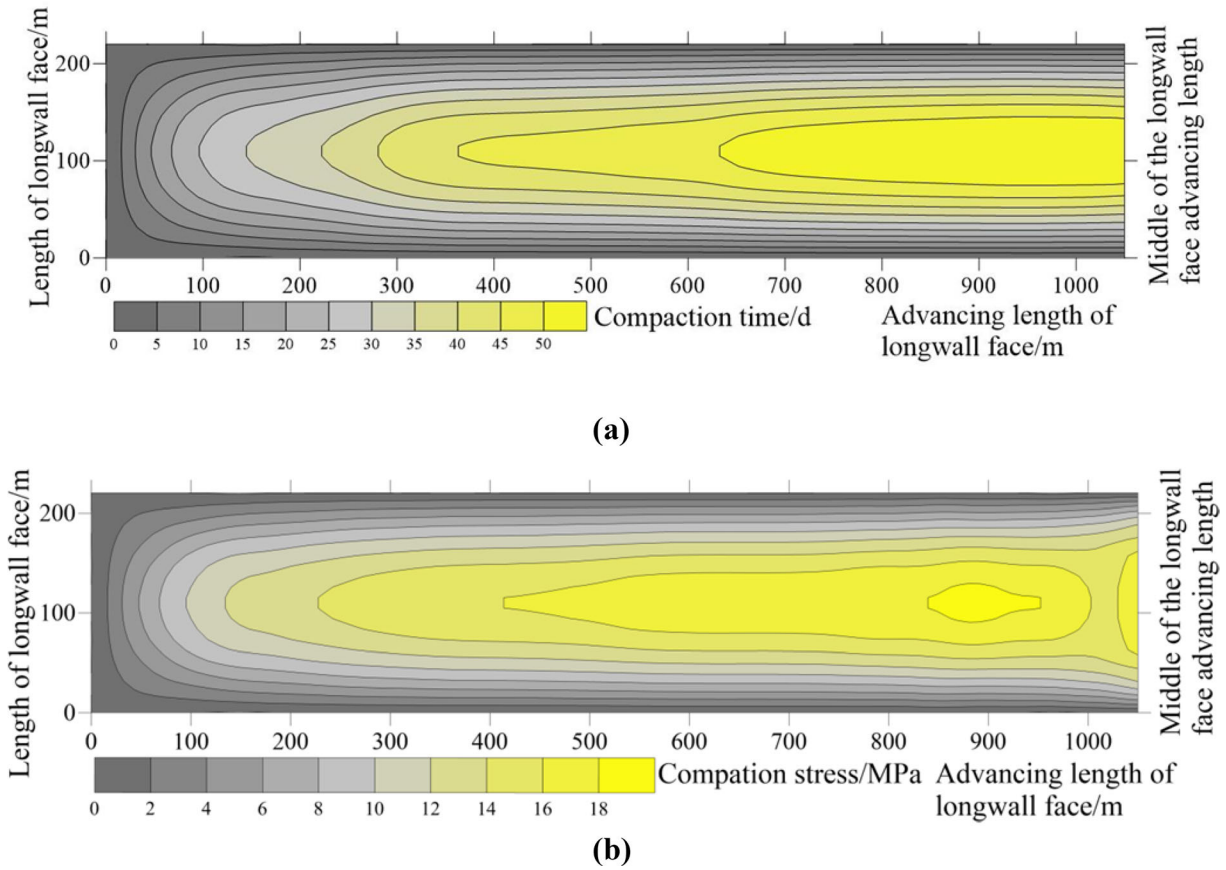
**(a)**

**(b)**

Figure 10. Compaction characteristics distribution of the caving zone: (**a**) compaction time; (**b**) compaction stress.
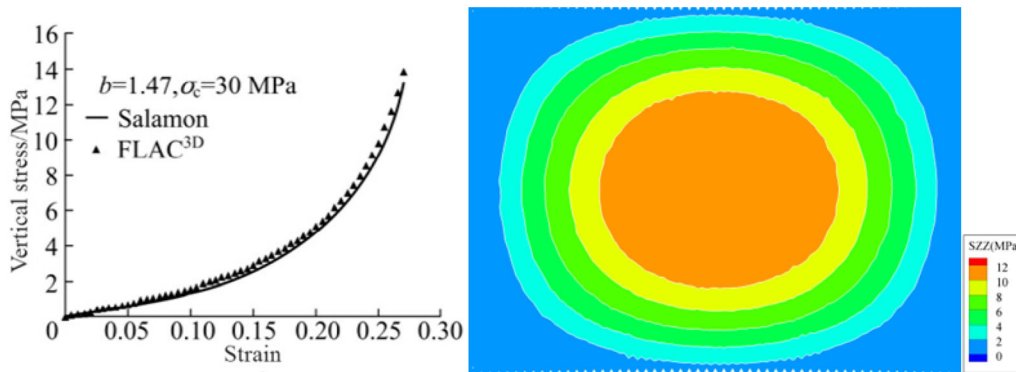


Figure 11. Numerical simulation results for compaction characteristics of caving zone in the gob.

$$\sigma_v = \frac{E_0\varepsilon}{(1 - \varepsilon/\varepsilon_m)} \quad (2)$$

In Eq. 2, $\sigma_v$ is vertical stress, $\varepsilon$ is vertical strain and $\varepsilon_m$ is maximum vertical strain. As can be seen

from Figure 11, the numerical simulation results are consistent with the measured results (Fig. 10b). However, it can be seen from the results of numerical simulation that compaction stress in the middle of caving zone ranging from 10 to 12 MPa is less

than the measured stress of 16–18 MPa in the middle of the caving zone. The main reason for this is that the advancing distance in the numerical simulation is only 350 m. According to the formula of advancing distance and compaction stress in Figure 9b, the maximum compaction stress at 175 m in the middle of numerical simulation caving zone can be calculated as 12.61 MPa. This is consistent with the numerical simulation results, and it further shows that the advancing distance of working face has influence on the degree of compaction of caving zone. In addition, compared to Figure 10, there is a positive correlation between compaction stress and compaction time in Figure 12. Using the linear formula in Figure 12, the compaction time needed for the stability of the caving zone can be deduced according to the compaction stress after caving zone stability obtained from the numerical simulation results.

## RESULTS AND DISCUSSION

To study the correlation between the permeability and the measured vertical stress in the caving zone, the compaction stress obtained from the compaction process of the caving zone and the permeability obtained from the permeability model are drawn in Figure 13. It can be seen from this figure that the vertical stress of the caving zone around each GGV increases gradually with the increase in compaction time, but the permeability decreases. The vertical stress of the caving zone presents an ''S''-type distribution as compaction time increases. That is, with the increase in com-
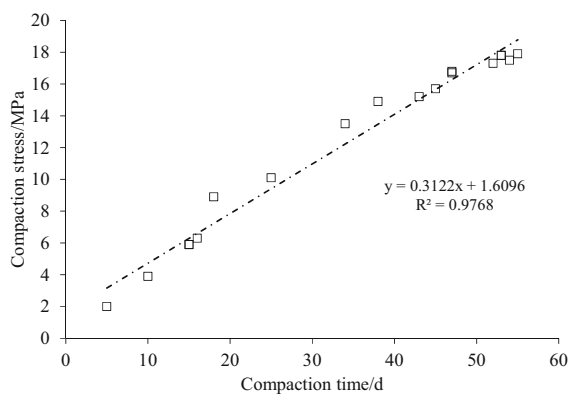


**Figure 12.** Relationship between compaction stress and compaction time.

paction time, the vertical stress first increases slowly, then sharply increases, and finally increases slowly until it stabilizes. This is consistent with the qualitative analysis results of vertical stress in the caving zone by Zhang et al. (2016), namely the caving zone began to be in a state of scattered accumulation, the broken coal and rock mass did not reach the roof, and the vertical stress increased slowly. With the increase in the advancing distance, the vertical stress increases sharply with roof subsidence and compacting broken coal and rock. After that, the overlying strata gradually stabilized, and the vertical stress in the caving zone gradually reached a stable state.

The vertical stress around each GGV exists quite differently. After reaching the stable stage, the vertical stresses at the four GGVs are 10.1 MPa, 15.2 MPa, 16.7 MPa and 17.3 MPa, respectively. The corresponding stable permeability is 715 m d, 332 m d, 319 md and 299 m d, respectively. The corresponding compaction time is 25 d, 43 d, 47 d and 52 d, respectively. These are consistent with the compaction times obtained from the above permeability calculation model. Thus, the permeability in the caving zone is related to the vertical stress: the longer the compaction time is, the greater the vertical stress is and the smaller the permeability is.

Direct field measurements of compacted stress and permeability in the caving zone are difficult. Thus, numerical simulations, laboratory experiments and theoretical models are the main means to study the relationship between stress and permeability of the caving zone. For numerical simulation, empirical formulas for volume strain of broken coal and rock and permeability are adopted to simulate the permeability changes in the caving zone (Whittles et al. 2006; Esterhuizen and Karacan 2007; Zhang et al. 2016). For the theoretical models, Carman–Kozeny and Happel equations can be used to calculate the permeability of the caving zone. For the laboratory experiments, the stress-permeability test of broken coal and rock is carried out by many researchers (Pappas and Mark 1993; Zhang et al. 2019). To compare the field test results with other methods, the simulation results by Zhang et al. (2016), the laboratory test results by Zhang et al. (2019), the theoretical models of Carman–Kozeny and Happel and the field test results are shown in Figure 14. In the figure, the permeability calculated by Carman–Kozeny and Happel equations and numerical simulation were smaller than the field measurements and laboratory tests, especially when the stress is greater
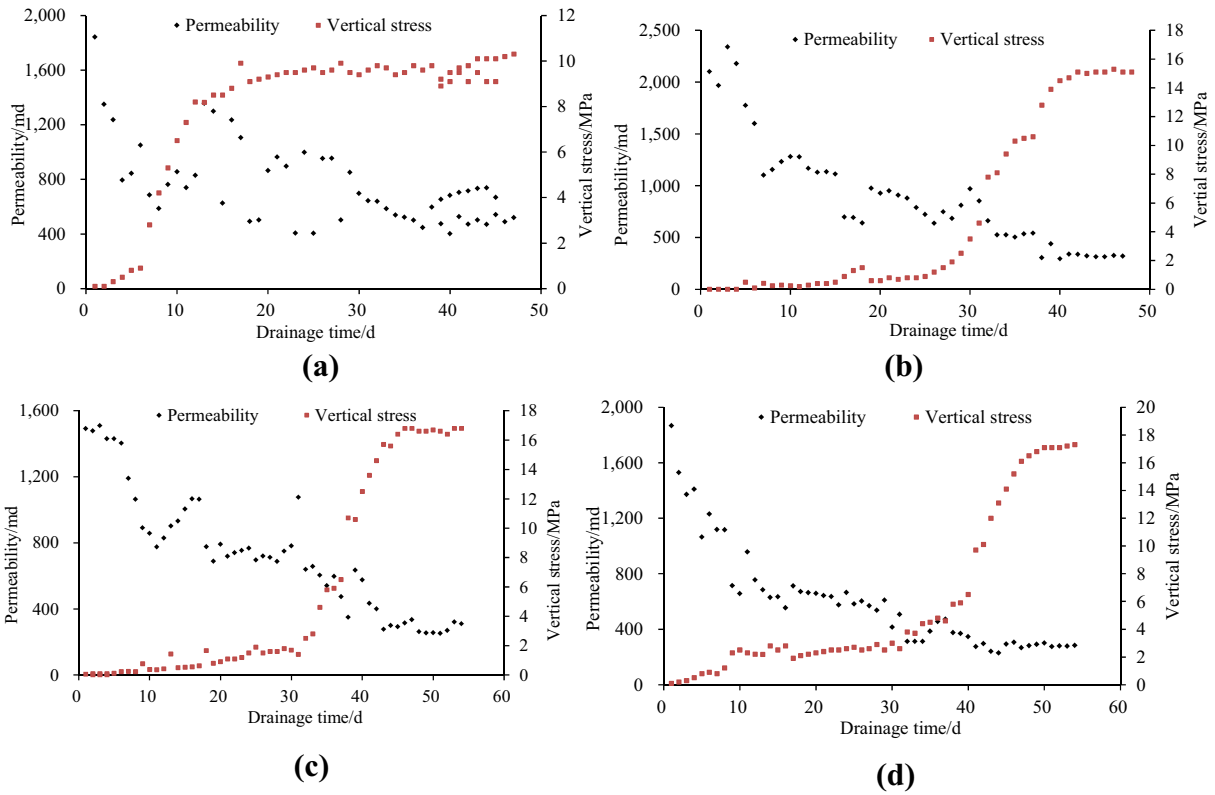
**Figure 13.** Vertical stress measurements and permeability changes of GGV in the caving zone: (**a**, **b**, **c**) and (**d**) 1–4 GGVs, respectively.
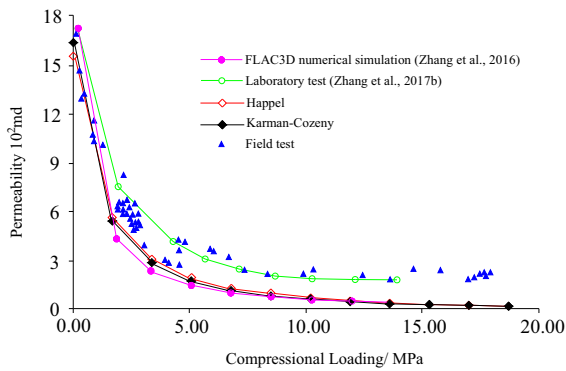


**Figure 14.** Contrasting results of the permeability calculation model and other theoretical models.

than 5 MPa. When the stress is close to 20 MPa, the theoretical and simulated permeability is close to 0. This is mainly due to the negative exponential formula used by the Carman–Kozeny and Happel formulas. When the vertical stress rises, the permeability decreases continuously and does not take into account the fact that the compressibility of the caving zone decreases with the increase in effective stress. Therefore, values from the Carman–Kozeny and Happel formulas are obviously different from the measured results. The laboratory test results are in good agreement with the field measurements. This indicates that the laboratory testing can represent the actual situation well.

## CONCLUSIONS

The permeability evolution of the caving zone can be divided into a gradually compaction stage and a compaction stable stage with the advancing of the longwall face. Because the distance from the edge of the caving zone is different, the advancing distance and compaction time required for the caving zone to reach stability are different. The farther the edge of the caving zone is, the longer the compaction time needed. This is also confirmed by numerical simulation results. Compaction time is also affected by the advancing speed of the longwall

face. The higher the speed of the longwall face is, the longer the compacting time is, but the effect is reduced. The permeability of the caving zone after compaction presents a horizontal "O"-type distribution, and the permeability from the inside to the outside is increased in turn.

The distribution characteristics of compaction stress and compaction time in the caving zone are obtained. The closer to the edge of the caving zone, the lower the compaction degree is, the smaller the compacting stress is, and the shorter the compaction time required to reach the stress is. Meanwhile, the quantitative relationship between the compaction degree (compaction stress and compaction time) of the caving zone and the distance from the edge of the caving zone is given, and the compaction stress and time increased with the distance by a negative exponential function. There is a linear relationship between compaction time and stress of the caving zone after it compacted. Based on this linear formula, the time needed for the compaction stability of the caving zone can be deduced according to the compaction stress obtained from the numerical simulation results.

During the compaction process of the caving zone, the compaction stress presents "S"-type distribution as compaction time increases. That is, with the increase in the compaction time, the vertical stress first increases slowly, then sharply increases, and then increases slowly until it stabilizes. The permeability in the caving zone after it is compacted depends on the compaction stress. There is a negative exponential relationship between permeability and compacted stress. Compared to the theoretical model and the numerical simulation, laboratory testing can provide measurements closer to field measured results.

## ACKNOWLEDGMENTS

## REFERENCES

Baptiste, N., & Chapuis, R. P. (2015). What maximum permeability can be measured with a monitoring well? *Engineering Geology, 184,* 111–118.

Barrash, W., Clemo, T., Fox, J. J., & Johnson, T. C. (2006). Field, laboratory, and modeling investigation of the skin effect at wells with slotted casing, Boise Hydrogeophysical Research Site. *Journal of Hydrology, 326*(1), 181–198.

Booth, C. J., & Greer, C. B. (2011). Application of MODFLOW using TMR and discrete-step modification of hydraulic properties to simulate the hydrogeologic impact of longwall mining subsidence on overlying shallow aquifers. In *Proceedings, mine water—Managing the challenges, Aachen, Germany* (pp. 211–215).

Cheng, G., Ma, T., Tang, C., Liu, H., & Wang, S. (2017). A zoning model for coal mining-induced strata movement based on microseismic monitoring. *International Journal of Rock Mechanics and Mining Sciences, 94,* 123–138.

Deng, K. Z., Tan, Z. X., Zhang, H. Z., Fan, H. D., & Zhang, L. Y. (2012). Research on calculating method of residual subsidence of longwall goaf. *Journal of the China Coal Society, 37*(10), 1601–1605.

Esterhuizen, G. S., & Karacan, C. Ö. (2007). A methodology for determining gob permeability distributions and its application to reservoir modeling of coal mine longwalls. In *2007 SME annual meeting, Denver, CO.*

Fan, L., & Liu, S. (2017). A conceptual model to characterize and model compaction behavior and permeability evolution of broken rock mass in coal mine gobs. *International Journal of Coal Geology, 172,* 60–70.

Jozefowicz, R. R. (1997). *The post-failure stress-permeability behaviour of coal measure rocks.* Doctoral dissertation, University of Nottingham.

Karacan, C. Ö. (2010). Prediction of porosity and permeability of caved zone in longwall gobs. *Transport in Porous Media, 82*(2), 413–439.

Lan, Z. Q., & Zhang, G. S. (2007). Numerical simulation of gas concentration field in multi-source and multi-congruence goaf. *Journal of China Coal Society, 32*(4), 396–401.

Li, J. M., Fei, L., Wang, H. Y., Zhou, W., Liu, H. L., Zhao, Q., et al. (2008). Desorption characteristics of coalbed methane reservoirs and affecting factors. *Petroleum Exploration and Development, 35*(1), 52–58.

Li, X. Y., & Logan, B. E. (2001). Permeability of fractal aggregates. *Water Research, 35*(14), 3373–3380.

Liang, B., Wang, B., Jiang, L., Li, G., & Li, C. (2016). Broken expand properties of caving rock in shallow buried goaf. *Journal of China University of Mining and Technology, 45*(3), 475–482.

Liu, W., Li, Y., Yang, C., Daemen, J. J., Yang, Y., & Zhang, G. (2015). Permeability characteristics of mudstone cap rock and interlayers in bedded salt formations and tightness assessment for underground gas storage caverns. *Engineering Geology, 193,* 212–223.

Meng, Z. P., Zhang, J., Shi, X. C., Tian, Y. D., & Li, C. (2016a). Calculation model of rock mass permeability in coal mine goaf and its numerical simulation analysis. *Journal of China Coal Society, 41*(8), 1997–2005.

Meng, Z. P., Zhang, J., Shi, X. C., Tian, Y. D., & Li, C. (2016b). Calculation model of rock mass permeability in coal mine goaf and its numerical simulation analysis. *Journal of China Coal Society, 41*(8), 1997–2005.

Palchik, V. (2003). Formation of fractured zones in overburden due to longwall mining. *Environmental Geology, 44*(1), 28–38.

Palchik, V. (2010). Experimental investigation of apertures of mining-induced horizontal fractures. *International Journal of Rock Mechanics and Mining Sciences, 47*(3), 502–508.

Pappas, D. M., & Mark, C. (1993) Behavior of simulated longwall gob material. Report of Investigations RI No. 9458, US Department of Interior, US Bureau of Mines.

Qin, Z., Yuan, L., Guo, H., & Qu, Q. (2015). Investigation of longwall goaf gas flows and borehole drainage performance by CFD simulation. *International Journal of Coal Geology, 150,* 51–63.

Salamon, M. D. G. (1991, January). Displacements and stresses induced by longwall mining in coal. In *7th ISRM congress. International society for rock mechanics.*.

Schatzel, S. J., Krog, R. B., & Dougherty, H. N. (2012). Methane emissions and airflow patterns on a longwall face. In *SME annual meeting* **(preprint)**.

Wang, B., Liang, B., Jiang, L., Li, G., & Li, C. (2015). Research on fractal calculation and application of water storage in void of caving rock in the goaf. *Chinese Journal of Rock Mechanics and Engineering, 34*(7), 1444–1451.

Whittles, D. N., Lowndes, I. S., Kingman, S. W., Yates, C., & Jobling, S. (2006). Influence of geotechnical factors on gas flow experienced in a UK longwall coal mine panel. *International Journal of Rock Mechanics and Mining Sciences, 43*(3), 369–387.

Xia, T., Wang, X., Zhou, F., Kang, J., Liu, J., & Gao, F. (2015). Evolution of coal self-heating processes in longwall gob areas. *International Journal of Heat and Mass Transfer, 86,* 861–868.

Yavuz, H. (2004). An estimation method for cover pressure re-establishment distance and pressure distribution in the goaf of longwall coal mines. *International Journal of Rock Mechanics and Mining Sciences, 41*(2), 193–205.

Zhang, C., Tu, S., Bai, Q., Yang, G., & Zhang, L. (2015). Evaluating pressure-relief mining performances based on surface gas venthole extraction data in longwall coal mines. *Journal of Natural Gas Science and Engineering, 24,* 431–440.

Zhang, C., Tu, S., Zhang, L., Bai, Q., Yuan, Y., & Wang, F. (2016). A methodology for determining the evolution law of gob permeability and its distributions in longwall coal mines. *Journal of Geophysics and Engineering, 13*(2), 181–193.

Zhang, C., Tu, S., & Zhao, Y. (2019). Compaction characteristics of the caving zone in a longwall goaf: A review. *Environmental Earth Sciences, 78*(1), 27–46.

Zhao, Y., Zhang, J., Chou, C. L., Li, Y., Wang, Z., & Ge, Y. (2008). Trace element emissions from spontaneous combustion of gob piles in coal mines, Shanxi, China. *International Journal of Coal Geology, 73*(1), 52–62.

Zhou, F. B., Xia, T. Q., Liu, Y. K., Hu, S. Y., & Zhang, Z. G. (2010). A calculation model for gas flow rates in surfaces boreholes extracting gas from pressure-relieved seams and gobs. *Journal of China Coal Society, 35*(10), 1638–1643.

Zhu, G., Xu, Z., Chen, X., & Ying, G. (2014). Study of influence functions of surface residual movement and deformation above old goaf. *Chinese Journal of Rock Mechanics and Engineering, 33*(10), 1962–1970.